EASY TWO-PHOTON IMAGE-SCANNING MICROSCOPY WITH SPAD ARRAY AND BLIND IMAGE RECONSTRUCTION

S. V. KOHO[1,2,†,*], E. SLENDERS[1,3,†], G. TORTAROLO[1,4], M. CASTELLO[1], M. BUTTAFAVA[5], F. VILLA[5], E. TCARENKOVA[1,2], M. AMELOOT[3], P. BIANCHINI[6], C.J.R. SHEPPARD[6], A. DIASPRO[6,7], A. TOSI[5], G. VICIDOMINI[1,*]

[1]MOLECULAR MICROSCOPY AND SPECTROSCOPY, ISTITUTO ITALIANO DI TECNOLOGIA, GENOA, ITALY
[2]UNIVERSITY OF TURKU, DEPARTMENT OF CELL BIOLOGY AND ANATOMY, INSTITUTE OF BIOMEDICINE AND MEDICITY RESEARCH LABORATORIES, LABORATORY OF BIOPHYSICS, TURKU, FINLAND
[3]HASSELT UNIVERSITY, BIOMEDICAL RESEARCH INSTITUTE (BIOMED), DIEPENBEEK, BELGIUM
[4]DIPARTIMENTO DI INFORMATICHE, BIOINGEGNERIA, ROBOTICA E INGEGNERIA DEI SISTEMI, UNIVERSITY OF GENOA, ITALY
[5]DIPARTIMENTO DI ELETTRONICA, INFORMAZIONE E BIOINGEGNERIA, POLITECNICO DI MILANO, MILAN, ITALY
[6]NANOSCOPY AND NIC@IIT, ISTITUTO ITALIANO DI TECNOLOGIA, GENOA, ITALY
[7]DIPARTIMENTO DI FISICA, UNIVERSITY OF GENOA, GENOA, ITALY
[†]THESE AUTHORS CONTRIBUTED EQUALLY TO THIS WORK
[*]TO WHOM CORRESPONDENCE SHOULD BE ADDRESSED; E-MAIL: SAMI.KOHO@IIT.IT, GIUSEPPE.VICIDOMINI@IIT.IT

Abstract. Two-photon excitation (2PE) microscopy is the imaging modality of choice, when one desires to work with thick biological samples, possibly *in-vivo*. However, the resolution in two-photon microscopy is poor, below confocal microscopy, and the lack of an optical pinhole becomes apparent in complex samples as reduced quality of optical sectioning. Here, we propose a straightforward implementation of 2PE image scanning microscopy (2PE-ISM) that, by leveraging our recently introduced ISM platform – based on a new single-photon avalanche diode array detector – coupled with a novel blind image reconstruction method, is shown to improve the optical resolution, as well as the overall image quality in various test samples. Most importantly, our 2PE-ISM implementation requires no calibration or other input from the user – it works like any old and familiar two-photon system, but simply produces higher resolution images (in real-time). Making the complexity disappear, in our view, is the biggest novelty here, and the key for making 2PE-ISM mainstream.

Introduction

Since the introduction of super-resolution methods (*1–3*), fluorescence microscopy research has been experiencing somewhat of a renaissance. A plethora of new optical microscopy techniques have been introduced, some able to reach resolution of only a few nanometers (*4–6*), a scale that was previously available only to electron microscopy. However, despite the big technological advances and promising proof-of-concept demonstrations, super-resolution microscopes have not been able to replace traditional fluorescence, confocal and two-photon

excitation (2PE) microscopes as go-to imaging tools in pre-clinical research (*7*). The old techniques are reliable, simple, familiar, highly compatible with all kinds of fluorescence labels and work well with many types of samples – whereas current super-resolution microscopes fall short on at least some of these characteristics.

Structured Illumination Microscopy (SIM) encompasses a collection of super-resolution implementations that make use of structured excitation (*3, 8*). In contrast to many other super-resolution methods, SIM does not require any special sample preparation (*9*). In its original form, SIM was implemented in a wide-field microscope, by projecting a striped illumination pattern with a line spacing close to the diffraction limit onto the sample, thereby shifting high-frequency information of the sample into the pass-band of the objective. Because the excitation pattern is diffraction limited, the maximum resolution gain obtainable with linear SIM techniques is a factor of two (*3*). The same resolution can theoretically be obtained in confocal laser scanning microscopy by completely closing the pinhole (*10*), but at the cost of extremely low signal-to-noise ratio. Image Scanning Microscopy (ISM) (*11*) can be considered as point-scanning SIM (*12*), in which the diffraction limited excitation laser spot is used as the SIM illumination pattern. Several implementations for ISM have been proposed (*13–18*), some relying on *a-posteriori* image reconstruction (e.g., pixel reassignment), and others on all-optical image reconstruction, to produce the ISM result image. The all-optical image reconstruction is achieved by optically enlarging the result image by factor of two with respect to the laser scanning grid. Some ISM architectures implement multi-spot excitation to increase imaging speed (*16, 17*). ISM shows great promise for becoming the next generation default imaging tool, since it works much like a closed-pinhole confocal would, but without the loss of signal.

Today, most ISM configurations are implemented with one-photon excitation, which limits the practically attainable imaging depth in thick biological samples, due to extensive scattering of the illumination light. Recently, to address this issue, ISM implementations employing 2PE have been proposed (*19, 20*). Zeiss also demonstrated the extension of their commercial Airyscan ISM system to 2PE (*21*). 2PE is well known to allow a much deeper penetration, and the infrared excitation light is also less phototoxic, as biological samples do not commonly absorb it (*22–24*). Moreover, the two-photon excitation process improves the optical sectioning capability to the extent that a separate pinhole is not usually necessary (*25*). The current 2PE-ISM implementations, however, are rather complex and cannot easily be integrated into regular point-scanning microscopy architectures. Moreover, the all-optical ISM methods require calibration measurements prior to every imaging session, which is both tedious as well as error-prone, as the imaging conditions in the actual samples, especially in depth and in the presence of aberrations, cannot be expected to be similar to thin and transparent calibration samples (*26*).

Recently, we proposed a new ISM platform based on a single-photon avalanche diode (SPAD) array detector (*27*) that, we hope, will speed up the transition from diffraction limited (point-scanning) systems to super-resolution microscopy. Here, based on this new platform, we present a very natural and straightforward ISM implementation with two-photon fluorescence excitation, which in theory can be implemented on any regular point-scanning microscope. In fact, as shown in (Fig. 1 a)), our implementation is essentially just a simple

upgrade to a confocal microscope, with only a couple of additional lenses and the new SPAD array detector. The same system can be used for multi-photon (as well as for single-photon) ISM with the SPAD array; or, alternatively, classical point detectors can be used. The SPAD array was placed as close as possible to the galvo mirrors to optimize for signal level and to properly conjugate the array detector with the object/image plane.

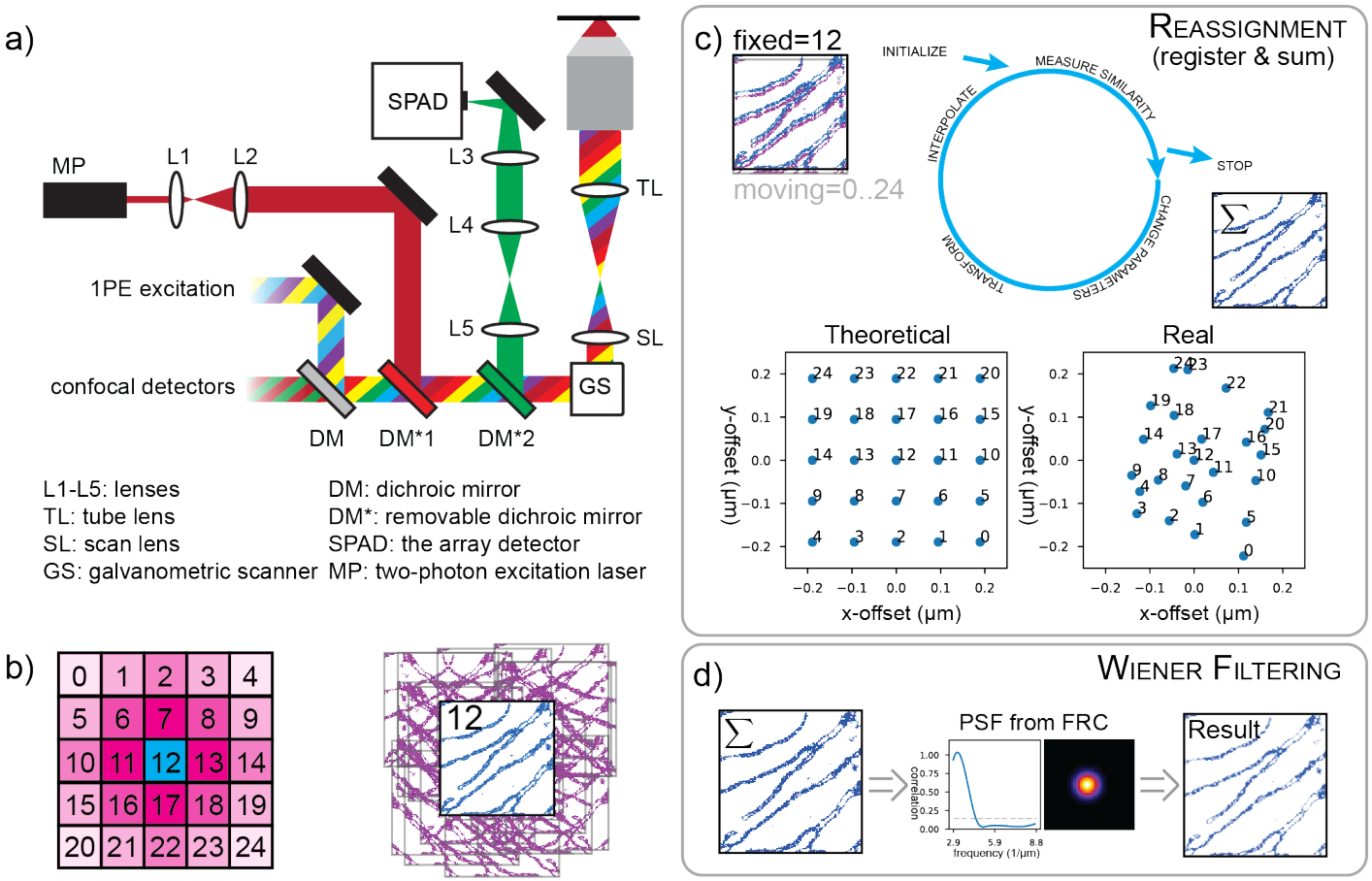

FIG. 1. **Description of the 2PE-ISM system**. In a) a schematic of the 2PE-ISM system is shown. The ISM part was built as an extension to a regular confocal microscope with several laser lines and detectors. Only three additional lenses (L3-L5) and a dichroic mirror (DM*2) are needed to convert a confocal/2PE system into a ISM super-resolution microscope. The dichroic mirrors DM*1-2 can be reconfigured to enable ISM imaging with the visible excitation lines. In b) an illustration of the pixel matrix of the SPAD array is shown. The pixels are numbered from 0-24, starting from the upper left corner. At the end of a scan, an image can be associated with each pixel position of the array. Each image is shifted with respect to the central detector element (12) image. In c) the adaptive pixel reassignment workflow is illustrated. First our iterative image registration method is applied to align all the individual images with the image from the central detector element (12). After registration, the images are added together to form the regular pixel reassignment result. The actual (Real) shifts are quite different from those suggested by theory (Theoretical), as shown by the two scatter plots. In order to take full advantage of the additional bandwidth of the ISM, as shown in d), a blind Wiener filter is applied on the reassignment result; the PSF is estimated from the ISM reassignment result image with FRC.

As already discussed for all-optical methods (*26*), proper alignment and fusion of the sub-images is essential for optimal functioning of an ISM microscope. A big advantage of our ISM implementation is that all the raw data is automatically recorded, without speed concerns and large data overhead that hampered the early camera-based ISM implementations. In (*27*) we proposed an adaptive ISM reconstruction method, in which image shifts are estimated directly from the data, by Fourier domain phase-correlation based method. For the 2PE-ISM, we implemented a more robust, completely blind ISM reconstruction method, which requires no calibration measurements or any prior knowledge of the sample or microscope configuration. We show how our algorithm allows improving the resolution – typically up-to the theoretical limit – as well as the optical sectioning in a variety of samples. We also propose a simple algorithm that makes it possible to construct the ISM result image in real-time, pixel-by-pixel for *live* visualisation.

The simple optical configuration, the novel image reconstruction methods and the real-time reassignment in our view are rather important steps towards the larger adoption of ISM, as they entirely hide its complexity; ideally the end user would just see a regular confocal or 2PE microscope, with improved resolution.

Results

ISM image reconstruction. ISM image reconstruction consists of two tasks: image registration and image fusion. Image registration is used to align the 25 sub-images (Fig. 1b)) into a common coordinate system, whereas image fusion is used to combine the registered sub-images into a single result image.

A new iterative image registration method is proposed, based on software originally developed for Tomographic STED microscopy image reconstruction (*28*). In image registration one tries to find a spatial transformation that aligns the details in two images as closely as possible. In iterative image registration, as illustrated in (Fig. 1c)) the search for the optimal spatial transformation is considered an optimisation problem: one image, called *fixed image*, is used as a reference, while a second image, called *moving image*, is translated until the details in the two images match. The images are considered to match when a chosen similarity *metric* reaches its maximum value. In our ISM registration implementation, the central detector image is always used as the *fixed image* and the 24 other images are sequentially registered with it.

After the shifts for all the 24 images have been calculated, images can be added together to produce the adaptive pixel reassignment ISM (APR-ISM). However, both in ISM and SIM some form of deconvolution or frequency domain filtering (re-weighting) is commonly used in order to maximise the effective resolution (e.g. (*3, 16, 18–20*)). To this end, as illustrated in (Fig. 1d)), we apply our blind Fourier Ring Correlation (FRC) based Wiener filtering approach (*29*) to the APR-ISM image; no prior knowledge of the point-spread-function (PSF) is needed, but it is estimated directly from the APR-ISM result image. Henceforth, we denote the combination of APR-ISM with blind deconvolution/Wiener filtering as APR-ISM^{b+}. The image shifting and Wiener filtering could be alternatively combined, as is done in SIM (*3, 30*), but we preferred to keep the two tasks separated here, e.g. in order to enable straightforward sub-pixel registration as well as the possibility to re-sample the resulting image into a different pixel size with respect to the raw data, and to support more complex (deformable) spatial transforms that may become useful at a later date. In addition to the APR-ISM^{b+}

reconstruction method, we also propose a simple algorithm that allows constructing the ISM result image point-by-point during data-acquisition, similarly to regular confocal or 2PE microscopes (Note S 1). This is possible because our SPAD array detector has no frame rate, and thus every single photon can in real time be assigned to its correct spatial location.

Benchmark measurements using test samples. In order to get an idea of the performance of our 2PE-ISM system, we took some benchmark measurements under ideal imaging conditions, with two very common microscope test samples: 1) a sample of 100 nm yellow-green carboxylate modified fluorescent nanospheres, and 2) a sample of fixed human breast tumor cells, cell line MDA–MB–231, stained with an alpha–tubulin antibody and with a Star488 secondary antibody.

In (Fig. 2 a)) four images of the nanoparticle sample are compared: a regular two-photon image (2PE), a two-photon image with a pinhole (2PE ph.), ISM result image after our adaptive pixel reassignment (APR-ISM) and the Wiener filtered ISM result image (APR-ISM^{b+}). The 2PE image was obtained by summing the signal from all SPAD array elements, without applying any shifts, whereas the 2PE ph. image corresponds to the image in the central detector element (pixel no 12 in Fig. 1 b)); the pixel itself works as a pinhole of approximately 0.5 Airy units in size. For the ISM image reconstruction, the 25 sub-images were first registered and then summed. The ISM shift vectors obtained with image registration are shown in a (x,y) scatter plot in (Fig. 2 a)). Interestingly, while the shifts clearly form a grid, as could be expected, already with a simple sample like beads, there are clearly some aberrations present and the grid is also somewhat tilted. The pixel no. 24 in the SPAD array used for the 2PE experiments is more noisy than the others, which appears to compromise the image registration with the sparse beads sample. As shown in the FRC measures in (Fig. 2 a)), the ISM pixel reassignment (APR-ISM) improved the resolution by a factor of ~ 2, which was further improved to factor of ~ 3 with our blind Wiener filter, applied on the reassignment result (APR-ISM^{b+}). The numerical resolution values obtained with FRC measurements on the nanoparticle sample (2PE: 312 nm, APR-ISM: 165 nm and APR-ISM^{b+}: 99 nm) correspond quite well with the theoretical FWHM values ($\mathrm{FWHM}_{2PE} = \frac{0.5\lambda}{\sqrt{2}\mathrm{NA}} = 239$ nm, for $\lambda_{2PE} = 950$ nm, NA $= 1.4$; $\mathrm{FWHM}_{2PEph} = 147$ nm, for $\lambda_{em} = 525$ nm) (*31*). Although the regular 2PE appears to perform somewhat sub-optimally, APR-ISM almost reaches the theoretical limit of a closed pinhole confocal (2PE ph.).

With the fixed cell sample, as demonstrated in (Fig. 2 b), the APR-ISM resolution is a factor of ~ 1.6 superior to the regular 2PE image, and blind Wiener filtering is able to recover ~ 2.5 fold resolution gain. It is worth noticing however that the resolution scale here is different than with the nanoparticles (2PE: 372 nm, APR-ISM: 223 nm and APR-ISM^{b+}: 155 nm); the 2PE resolution with the cell sample remains below, but is close to the Abbe's diffraction limit ($d_{min} = \frac{\lambda}{2\mathrm{NA}} = 339\ nm$, for $\lambda = 950$ nm, NA $= 1.4$; quadratic dependency with the intensity is not considered), and the APR-ISM resolution measures are in good agreement with previous reports on non-linear ISM (*19, 20*). We then tried to push the resolution in APR-ISM further by iterative Richardson-Lucy (RL) deconvolution (Fig. S 1). Although the RL is able to considerably boost the contrast, no major gains are made in terms of quantitative resolution. In (Fig. S 2) our real-time pixel reassignment algorithm

is shown to produce good results with the HeLa cell image, with similar level of details that were observed in (Fig.2 b)). A strong signal-to-noise ratio (SNR) gain is observed with respect to the 2PE ph. image, which helps to underline how, already with simple test samples such as the two shown here, introducing an optical pinhole (2PE ph.) has a strongly adverse effect on the SNR in 2PE microscopy. While the features clearly get smaller, as suggested by the theory (FWHM_{2PE_ph} *versus* FWHM_{2PE}), effective resolution values are actually worse than in regular 2PE. This underlines the strength of ISM, and of course helps to understand why optical pinholes are not typically implemented in 2PE microscopes.

In (Fig. S 3) we compare the ISM shifts obtained by image registration to theoretical values calculated with reassignment factor 0.5, which is based on the assumption that if the emission and excitation PSFs are equal and offset by vector $\hat{d}$, the ISM shift vector should be $-\hat{d}/2$ (*11, 13*). We used the 0.5 here, as it appears to be most commonly used in the literature, although recently it was theoretically estimated that the "optimal" reassignment factor in 2PE-ISM may be slightly larger (*32*). The principle of obtaining the theoretical shifts is illustrated in (Fig. S 4). The lengths of the real and theoretical shifts increase linearly as a function of distance from the central detector element, but few other similarities can be found. The data-based magnification estimates (Beads: 413, HeLa: 452) – slope of the linear model fit in (Fig. S 3 b)) – appear to be somewhat lower than the optical configuration (500). However, a comparison of ISM reassignment results – theoretical and adaptive – with the HeLa cell images (Fig. S 5) suggests that the 500x magnification is actually more correct. In any case, it is quite evident from (Fig. S 3 c)) that there is no "optimal" reassignment factor that would work with all images, as the effective image shifts strongly vary from image-to-image. Our APR-ISM reconstruction clearly produces the highest quality results, as it makes no assumptions of the reassignment factor, but instead estimates the image shifts directly from the data.

Diving into a hazy brain slice. A multi-photon microscope arguably is most at home with thick samples that are hard or impossible to image with regular fluorescence microscopy methods, and thus we decided to test our 2PE-ISM in such samples. A partially optically-cleared mouse brain that expresses YFP in neurons, was imaged at different penetration depths, up-to the maximum working distance of the microscope objective, $\sim 140\ \mu m$. As shown in (Fig. 3 a)) the 2PE-ISM is able to maintain rich details and good contrast all the way up to the maximum working distance. APR-ISM^{b+} practically provides a constant image quality across the imaging depths, by maintaining a spatial resolution of $\sim 170nm$, whereas the resolution in regular 2PE images degrades from 500 nm to 570 nm as a function of depth, as can be expected (see FRC measurements in (Fig. 3 b)); this translates to a resolution improvement of factor three to four. The resolution improvement with the regular pixel reassignment (APR-ISM) is a bit less dramatic, a factor of ~ 1.5. The numerical values are in good agreement with those obtained in (*19, 20*). The ISM reassignment also appears to improve the optical sectioning capability of the 2PE system, as the ISM results are sharper and show a much reduced amount of out-of-focus haze.

Looking at the ISM shift vectors in (Fig. 3 c)), our adaptive blind pixel reassignment appears to be doing much more than simply introducing a tiny virtual pinhole. As discussed in (*27*), the light distribution on the array

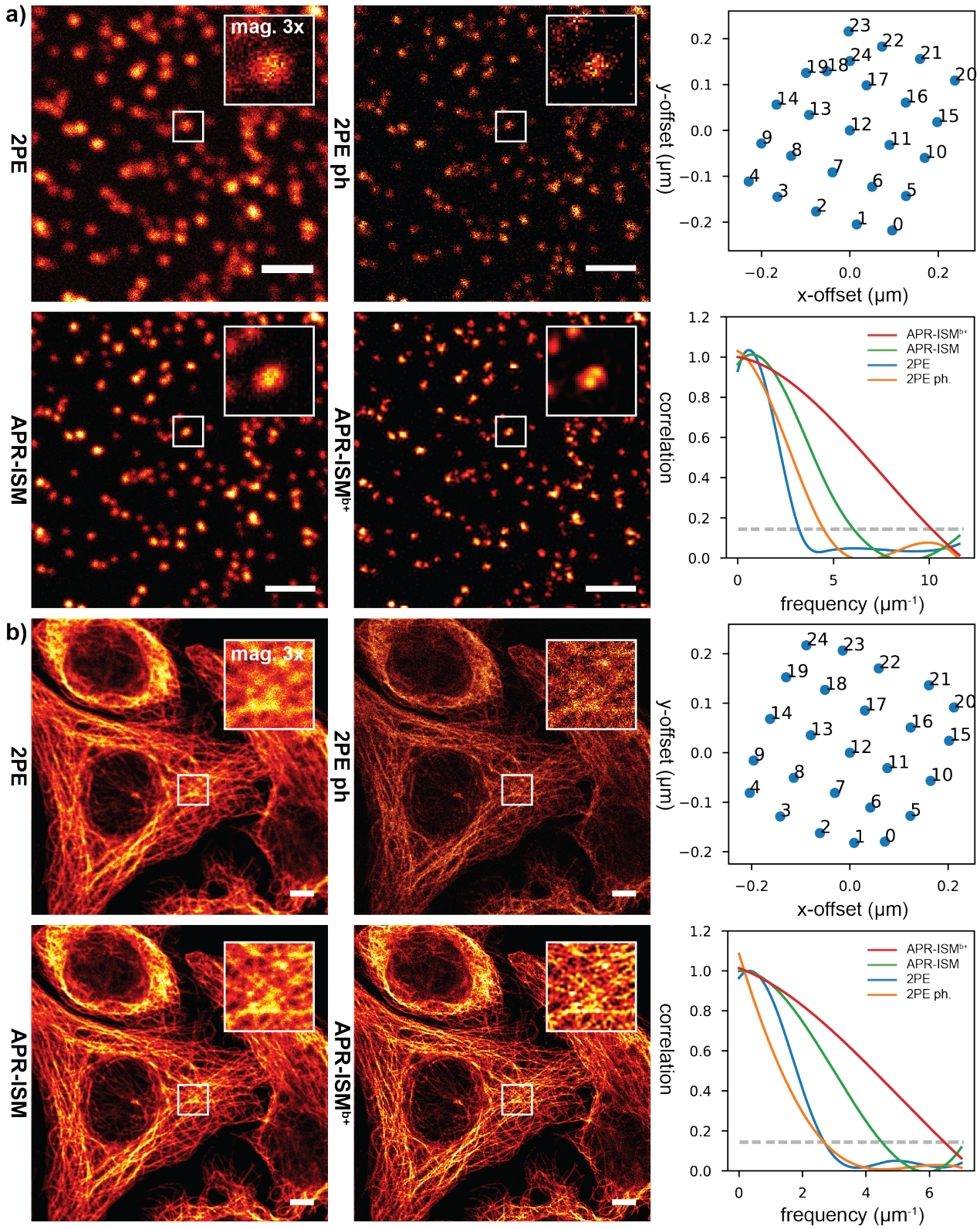

FIG. 2. textbf2PE-ISM imaging with simple test samples In a) results obtained with a d=100nm nanoparticle sample are shown. A nearly three-fold resolution improvement is observed with APR-ISM^{b+} compared to 2PE, as shown by FRC measurements. The sub-image shifts form a somewhat tilted grid. In b) similar results for a HeLa cell sample are shown. The sub-image shifts are similar to a), but a bit smaller, suggesting a larger PSF size, which is consistent with the resolution measurements. Scale bars: 2 μm (Beads); 4 μm (HeLa)

detector is related to the microscope's PSF, and thus changes in the PSF due to different sorts of aberrations will become visible as changes in the image shifts. In fact, it is actually possible to identify optical effects, such as coma (45 μm) and astigmatism (140 μm) in the ISM shift scatter plots in (Fig. 3 c)), when comparing the results to the ideal rectangular grid. Typically such effects are corrected during imaging with adaptive optics (*20*), but our adaptive blind ISM image reconstruction appears to enable correcting some aberrations at the post-processing stage as well. As shown in (Fig. S 3), the distribution of the lengths of the ISM shift vectors is also clearly less linear than with the Hela cell/Beads samples, which is also indicative of presence of aberrations; however, the phenomenon is much more evident in the 2D scatter plot of the ISM shifts.

Conclusion

In this paper, we introduced a 2PE-ISM system based on a SPAD array detector that, compared to current state-of-the art, is wonderfully simple: one can convert a regular confocal/2PE microscope into 2PE-ISM with only a couple of additional mirrors and lenses. In addition, thanks to the novel image reconstruction method, our 2PE-ISM microscope is very similar to use as a regular 2PE system, because no calibration measurements or other additional steps are required to achieve the improved resolution. While in this paper we focused on 2PE fluorescence imaging, the proposed architecture should also work in other non-linear (label-free) microscopy methods, such as Second Harmonic Generation (SHG) imaging; all-optical SHG-ISM was recently demonstrated in (*19*).

We demonstrated how our adaptive blind ISM image reconstruction is able to generate nearly constant quality, high resolution images, with different samples, and at various penetration depths. In addition to the accurate image alignment, the Wiener filtering (deconvolution) appears to be a crucial step, as otherwise the highest spatial frequencies remain too weak to be observed. In this work a very simple Wiener filtering approach was used – implementing more robust (multi-image) reconstruction methods that leverage the 25 independent observations, may in the future lead to further gains in image contrast and effective resolution.

In addition to the adaptive blind ISM image reconstruction method, a simple algorithm was proposed that allows generating a super-resolution ISM result image pixel-by-pixel for *live*-visualisation. This is an important step towards making ISM simple. The next important steps will be fully supporting 3D (stacks) and other scanning modes (XZ, YZ), as both of these features are commonly used in regular confocal and 2PE microscopes. Because all the raw data is saved in our 2PE-ISM implementation, it is possible to treat stacks as 25 individual 3D images, rather than a series of 2D images, as is the case in the all-optical techniques. This seems to be rather important, as based on a simple preliminary experiment with the Beads sample, the axial information is important and the axial shifts appear to be rather large (Fig. S 6). The results are especially interesting as there appears to be a strong resolution gain in the axial direction as well. In order to reach any conclusions however, further investigation is required.

The final thoughts as well as several examples in this paper, help to underline the importance of computation in modern microscopy. In wide-field microscopy, similar approaches have been in regular use already for a while – e.g. axial sectioning based on deconvolution, SIM, localization based super resolution – but confocal and 2PE

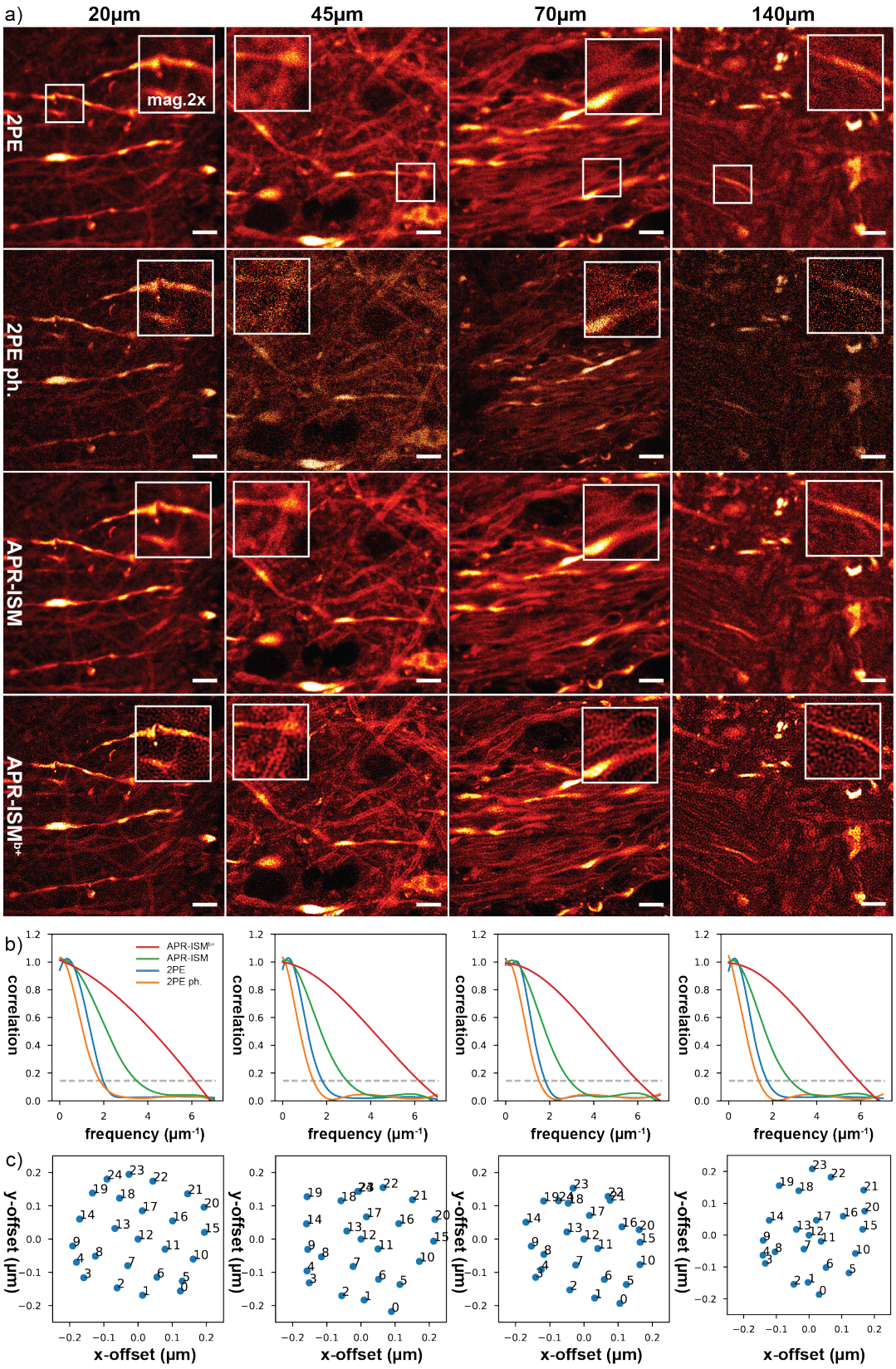

FIG. 3. **2PE-ISM imaging of a mouse brain**. In a) images are shown at different penetration depths (20 μm – 140m μm), for two-photon (2PE), two-photon with pinhole (2PE ph.), adaptive pixel reassignment (APR-ISM) and adaptive pixel reassignment with blind Wiener filtering (APR-ISM^{b+}). In b) FRC measures for the four types of images are compared at different imaging depths. In c) 2D scatter plots of the registration results (ISM shifts) are shown. Scale bars: 4 μm

microscopy have remained largely analog and microscope users often have to content with the raw data. We think that ISM with its massive information content, such as our 2PE-ISM, can put an end to that.

Materials & Methods

The Custom Microscope Setup. Our 2PE-ISM system was implemented as a modification to a confocal microscope, which itself is a modified Abberior Instruments RESOLFT system (Abberior Instruments, Germany). As shown in Figure 1, the femtosecond two-photon excitation laser (Chameleon Ti:Sapphire, Coherent) was coupled on the confocal microscope's common optical path via dichroic mirror DM*1 (720 nm SP, Semrock, USA). The fluorescence signal was directed to the SPAD array with a second dichroic mirror DM*2 (720nm LP, Semrock, USA). Both DM*1 and DM*2 are removable/exchangeable, which allows using the same microscope for single-photon ISM and regular confocal (spectroscopy) imaging. The lens pairs SL-L5 and L3-L4 conjugate the SPAD array with the object plane and adjust the magnification (~ 500), to give the SPAD array ~ 1.5 Airy unit field-of-view. A (512/40 nm, Semrock, USA) emission filter was installed in front of the SPAD array to block ambient light. The point-scanning was implemented using a galvanometric mirror XY scanner (6215H, Cambridge Technology, USA), coupled with $f = 50$ mm Leica scan lens and a $f = 250$ mm Leica tube lens. Axial scanning, as well as sample focusing, was implemented via a piezo stage (NanoMax MAX302, Thorlabs, USA). A single Leica Plan-Apochromat 100x/1.4-0.7 Oil CS (Leica Microsystems, Germany) objective was used in all experiments. The image acquisition was performed with our *Carma* microscope control software, which takes care of the real-time hardware control tasks (scanning, laser control etc.) as well as fluorescence signal recording from the 25 SPAD array pixels; the software also has a PC user interface for controlling the various functions of the microscope system and to preview and process the imaging results.

The ISM reconstruction method. The ISM image reconstruction is a two step process. First, all the sub-images (array pixels 1-25) need to be registered. Second, the registered sub-images need to be fused to produce a single result image.

In iterative image registration one image, called *fixed image*, is used as a reference, while a second image, called *moving image*, is translated until the details in the two images match. In our ISM registration implementation the central detector element image is always used as the *fixed image* and the 24 other images are sequentially registered with it. A rigid body spatial transformation was used, without rotation, which means that the registration entails the optimisation of two parameters. Higher level spatial transformations are supported as well in our open-source MIPLIB software library (see Acknowledgements), which may become useful for future experiments, e.g. in correcting strong aberrations. Deformable spatial transforms, in context of camera-based ISM were already discussed in (*26*); the proposed approaches naturally only work if separate images are acquired for every sampling position, which typically is not the case in all-optical ISM implementations.

The ISM image registration methods in our MIPLIB library leverage the Insight Toolkit (ITK) (*33*), a large open-source medical image processing toolkit. The image registration pipeline is divided into several components, each of which can be selected to suit the needs of the specific task: *metrics*, *optimizers*, *transforms*,

interpolators and *initializers*. The *metric* is used to measure the similarity of the *moving* and *fixed* images; the aim of a registration task is to maximize its value. The *optimizer* adjusts the *transform* parameters, until the similarity *metric* reaches its maximum value. The *interpolator* is used to calculate pixel values at non-grid positions during transformation. The *initializer* calculates the initial transformation for rough alignment of the *moving image* with the *fixed image*. The components of our ISM image registration implementation are:

metric: Normalised Cross Correlation that is calculated from 0.01-1% subset of the pixel values; a higher percentage is required for low quality or extremely sparse images. Different similarity metrics are also supported in the MIPLIB software.

optimizer: Regular Step Gradient Optimizer, which essentially at each iteration takes a step along the direction of the metric derivative

initializer: not needed (images are already sufficiently overlapped); both automatic and manual offset initialization is supported in MIPLIB software.

transform: 2D rigid translation transform. Scalable and deformable spatial transformations are supported as well, but not used here.

interpolator: linear interpolation

All registration and image transformation tasks in ITK/MIPLIB are performed in physical units (μm), which means that the images can be re-sampled to a different pixel size without changing the registration result. In ISM this is particularly useful, if the original data is sampled too sparsely to support the two-fold resolution improvement. One can also shrink the images before registration to increase speed and optimise memory consumption. The registration is also always sub-pixel: for the results shown in this work, the minimum *optimizer* step size was set to 0.5 nm.

After all the 25 images have been registered, they can be added together to for the regular APR-ISM pixel reassignment result. In order to take full advantage of ISM however, one has to still remove the blurring effect of the PSF, which in this case is that of the ISM reassignment result, as explained in context of SIM image reconstruction in (*30*). To this end, we applied our FRC based blind Wiener filter on the reassignment result. The filter first estimates the PSF directly from the image with an FRC measurement, after which a classical Wiener filter is applied; the FRC cut-off value is used as a full-width-half-maximum (FWHM) value for a Gaussian PSF. Please refer to (*29*) for a detailed description.

The ISM image reconstruction workflow described above is mainly intended for the post-processing stage. The pixel reassignment can, however, also be performed in real-time, pixel-by-pixel, just as in a regular confocal or two-photon microscope (Note S 1).

Resolution measurement. The resolution measurements shown in this work, were calculated with our one-image FRC. The principle is the same as with the blind image deconvolution: first an image is split into two sub-images, after which the FRC is taken with the two sub-images as inputs. The one-image FRC method is described in detail in (*29*)

Test Samples. We demonstrated the enhancement on spatial resolution of 2PE-ISM *via* imaging of fluorescent beads, tubulin filaments and optically cleared mouse brain.

Fluorescent beads: In this study we used Yellow/Green fluorescent nanoparticles with a diameter of 100 nm (FluoSpheres, ThermoFisher Scientific, USA).

Tubulin filaments in fixed cells: Human HeLa cells were fixed with ice-cold methanol for 20 min at 20 ℃ and then washed three times for 15 min in PBS. After 1 h at room temperature, the cells were treated in a solution of 3% bovine serum albumin (BSA) and 0.1% Triton in PBS (blocking buffer). The cells were then incubated with monoclonal mouse anti-α-tubulin antiserum (Sigma-Aldrich) diluted in blocking buffer (1:800) for 1 h at room temperature. The α-tubulin antibody was revealed by Abberior STAR488 goat anti-mouse (Abberior) for the custom microscope. The cells were rinsed three times in PBS for 5 min.

Optically cleared brain of Thy1-eYFP-H transgenic mouse: The CLARITY method was used to clear the mouse brain (*34*). In short, after perfusion, mouse brains were post-fixed in 4% PFA overnight at 4 ℃ and then immersed in 2% hydrogel (2% acrylamide, 0.125% Bis, 4% PFA, 0.025% VA-044 initiator (w/v), in PBS) for 3 days at 4 ℃. Samples were degassed and polymerized for 3.5 hours at 37 ℃. The samples were removed from hydrogel and washed with 8% SDS for 1 day at 37 ℃. The samples were transferred to fresh 8% SDS for 21 days at 37 ℃ for de-lipidation. Then the samples were washed with 0.2% PBST for 3 days at 37 ℃. Brains were incubated in RapiClear CS (Cat#RCCS002, SunJin Lab) for 2-3 days at room-temperature for the optical clearing.

References

1. S. W. Hell, J. Wichmann, Breaking the diffraction resolution limit by stimulated emission: stimulated-emission-depletion fluorescence microscopy. *Opt. Lett.* **19**, 780–782 (1994).
2. E. Betzig, G. H. Patterson, R. Sougrat, O. W. Lindwasser, S. Olenych, J. S. Bonifacino, M. W. Davidson, J. Lippincott-Schwartz, H. F. Hess, Imaging intracellular fluorescent proteins at nanometer resolution. *Science* **313**, 1642–1645 (2006).
3. M. G. L. Gustafsson, Surpassing the lateral resolution limit by a factor of two using structured illumination microscopy. *J. Microsc.* **198**, 82–87 (2000).
4. G. Shtengel, J. A. Galbraith, C. G. Galbraith, J. Lippincott-Schwartz, J. M. Gillette, S. Manley, R. Sougrat, C. M. Waterman, P. Kanchanawong, M. W. Davidson, R. D. Fetter, H. F. Hess, Interferometric fluorescent super-resolution microscopy resolves 3D cellular ultrastructure. *Proceedings of the National Academy of Sciences* **106**, 3125–3130 (2009).
5. F. Huang, G. Sirinakis, E. S. Allgeyer, L. K. Schroeder, W. C. Duim, E. B. Kromann, T. Phan, F. E. Rivera-Molina, J. R. Myers, I. Irnov, M. Lessard, Y. Zhang, M. A. Handel, C. Jacobs-Wagner, C. P. Lusk, J. E. Rothman, D. Toomre, M. J. Booth, J. Bewersdorf, Ultra-High resolution 3D imaging of whole cells. *Cell* **166**, 1028–1040 (2016).
6. F. Balzarotti, Y. Eilers, K. C. Gwosch, A. H. Gynnå, V. Westphal, F. D. Stefani, J. Elf, S. W. Hell, Nanometer resolution imaging and tracking of fluorescent molecules with minimal photon fluxes. *Science* **355**, 606–612 (2017).
7. A. Diaspro, *Confocal and Two-Photon Microscopy: Foundations, Applications and Advances*, Confocal and Two-Photon Microscopy: Foundations (Wiley-Liss, 2001).
8. F. Ströhl, C. F. Kaminski, Frontiers in structured illumination microscopy. *Optica, OPTICA* **3**, 667–677 (2016).
9. E. N. Ward, R. Pal, Image scanning microscopy: an overview. *J. Microsc.* **266**, 221–228 (2017).

10. C. J. R. Sheppard, A. Choudhury, Image formation in the scanning microscope. *Optica Acta: International Journal of Optics* **24**, 1051–1073 (1977).
11. C. J. R. Sheppard, Super-resolution in confocal imaging. *Optik* **80**, 53–54 (1988).
12. Y. Wu, H. Shroff, Faster, sharper, and deeper: structured illumination microscopy for biological imaging. *Nat. Methods* p. 1 (2018).
13. C. B. Müller, J. Enderlein, Image scanning microscopy. *Phys. Rev. Lett.* **104** (2010).
14. G. M. R. De Luca, R. M. P. Breedijk, R. A. J. Brandt, C. H. C. Zeelenberg, B. E. de Jong, W. Timmermans, L. N. Azar, R. A. Hoebe, S. Stallinga, E. M. M. Manders, Re-scan confocal microscopy: scanning twice for better resolution. *Biomed. Opt. Express* **4**, 2644–2656 (2013).
15. S. Roth, C. J. R. Sheppard, K. Wicker, R. Heintzmann, Optical photon reassignment microscopy (OPRA). *Optical Nanoscopy* **2**, 5 (2013).
16. A. G. York, P. Chandris, D. D. Nogare, J. Head, P. Wawrzusin, R. S. Fischer, A. Chitnis, H. Shroff, Instant super-resolution imaging in live cells and embryos via analog image processing. *Nat. Methods* **10**, 1122–1126 (2013).
17. O. Schulz, C. Pieper, M. Clever, J. Pfaff, A. Ruhlandt, R. H. Kehlenbach, F. S. Wouters, J. Großhans, G. Bunt, J. Enderlein, Resolution doubling in fluorescence microscopy with confocal spinning-disk image scanning microscopy. *Proc. Natl. Acad. Sci. U. S. A.* **110**, 21000–21005 (2013).
18. M. Castello, C. J. R. Sheppard, A. Diaspro, G. Vicidomini, Image scanning microscopy with a quadrant detector. *Opt. Lett.* **40**, 5355–5358 (2015).
19. I. Gregor, M. Spiecker, R. Petrovsky, J. Großhans, R. Ros, J. Enderlein, Rapid nonlinear image scanning microscopy. *Nat. Methods* **14**, 1087–1089 (2017).
20. W. Zheng, Y. Wu, P. Winter, R. Fischer, D. D. Nogare, A. Hong, C. McCormick, R. Christensen, W. P. Dempsey, D. B. Arnold, J. Zimmerberg, A. Chitnis, J. Sellers, C. Waterman, H. Shroff, Adaptive optics improves multiphoton super-resolution imaging. *Nat. Methods* **14**, 869–872 (2017).
21. Zeiss, Application note: Airyscan detection in multiphoton microscopy: super- resolution and improved signal-to-noise ratio beyond the confocal depth limit. *Nat. Methods* (2018).
22. W. R. Zipfel, R. M. Williams, W. W. Webb, Nonlinear magic: multiphoton microscopy in the biosciences. *Nat. Biotechnol.* **21**, 1369–1377 (2003).
23. F. Helmchen, W. Denk, Deep tissue two-photon microscopy. *Nat. Methods* **2**, 932–940 (2005).
24. K. T. Takasaki, J. B. Ding, B. L. Sabatini, Live-cell superresolution imaging by pulsed STED two-photon excitation microscopy. *Biophys. J.* **104**, 770–777 (2013).
25. W. Denk, J. H. Strickler, W. W. Webb, Two-photon laser scanning fluorescence microscopy. *Science* **248**, 73–76 (1990).
26. J. E. McGregor, C. A. Mitchell, N. A. Hartell, Post-processing strategies in image scanning microscopy. *Methods* **88**, 28–36 (2015).
27. M. Castello, G. Tortarolo, M. Buttafava, T. Deguchi, F. Villa, S. Koho, L. Pesce, M. Oneto, S. Pelicci, L. Lanzanó, P. Bianchini, C. J. R. Sheppard, A. Diaspro, A. Tosi, G. Vicidomini, A robust and versatile platform for image scanning microscopy enabling super-resolution FLIM. *Nat. Methods* (2019).
28. S. Koho, T. Deguchi, P. E. E. Hänninen, A software tool for tomographic axial superresolution in STED microscopy. *J. Microsc.* **260**, 208–218 (2015).
29. S. V. Koho, G. Tortarolo, M. Castello, T. Deguchi, A. Diaspro, G. Vicidomini, Fourier ring correlation simplifies image restoration in fluorescence microscopy (2019).
30. K. Wicker, *Super-Resolution Microscopy Techniques in the Neurosciences*, E. F. Fornasiero, S. O. Rizzoli, eds. (Humana Press, Totowa, NJ, 2014), pp. 133–165.

31. G. Cox, C. J. R. Sheppard, Practical limits of resolution in confocal and non-linear microscopy. *Microsc. Res. Tech.* **63**, 18–22 (2004).
32. C. J. R. Sheppard, M. Castello, G. Tortarolo, G. Vicidomini, A. Diaspro, Image formation in image scanning microscopy, including the case of two-photon excitation. *Journal of the Optical Society of America a-Optics Image Science and Vision* **34**, 1339–1350 (2017).
33. T. S. Yoo, M. J. Ackerman, W. E. Lorensen, W. Schroeder, V. Chalana, S. Aylward, D. Metaxas, R. Whitaker, Engineering and algorithm design for an image processing api: a technical report on ITK–the insight toolkit. *Stud. Health Technol. Inform.* **85**, 586–592 (2002).
34. K. Chung, J. Wallace, S.-Y. Kim, S. Kalyanasundaram, A. S. Andalman, T. J. Davidson, J. J. Mirzabekov, K. A. Zalocusky, J. Mattis, A. K. Denisin, S. Pak, H. Bernstein, C. Ramakrishnan, L. Grosenick, V. Gradinaru, K. Deisseroth, Structural and molecular interrogation of intact biological systems. *Nature* **497**, 332–337 (2013).

Acknowledgements

We thank Ryu Nakamura (Nikon Corporation, Japan) for support on brain imaging. We thank Ryu Nakamura (Nikon Corporation, Japan), Dr. Ryosuke Kawakami, Dr. Kohei Otomo, and Prof. Tomomi Nemoto (Research Institute for Electronic Science, Hokkaido University, Japan) for advise in whole brain imaging. We thank Dr. Michele Oneto (Istituto Italiano di Tecnologia, Italy) for support in cell preparation, Dr. Simonluca Piazza (Istituto Italiano di Tecnologia, Italy) for useful discussions.

Author contributions. S.K., E.S., and G.V. conceived the idea. S.K. and G.V. supervised the project, with support from C.J.R.S., A.D., and A.T.. E.S., S.K., E.T., G.T., P.B., and G.V. designed and implemented the custom 2PE-ISM system. S.K., G.T., and M.C., developed the image processing and analysis software. E.S. performed the experiments. S.K. analysed the data with support from all authors. M.C., G.T. and G.V. designed and developed the controlling architecture. M.C., M.B., F.V., A.T., and G.V., designed the SPAD array module. M.B., F.V., and A.T. realised and characterised the SPAD array module. S.K., E.S., and G.V. wrote the manuscript with input from all authors.

Financial disclosure. The authors thank FWO (Fonds voor Wetenschappelijk Onderzoek - Vlaanderen) for the financial support (travel grant V429717N and FWO project G092915). This project has received funding from the European Unions Horizon 2020 research and innovation programme under the Marie Skodowska-Curie grant agreement AdaptiveSTED No 794531.

Conflicts of interests. The authors declare no potential conflict of interests.

Code Availability. All the image analysis and processing methods used in this work are available as a part of the MIPLIB software library at (https://github.com/sakoho81/miplib)

Data availability. All the data that supports the findings of this study are available from the corresponding author upon request.

Supporting information

Fig. S1 Comparing blind Wiener and Richardson Lucy deconvolution with HeLa cell image

Fig. S2 Real-time reassignment

Fig. S3 Comparing theoretical and data-based ISM shifts

Fig. S4 Describing how theoretical ISM shifts are calculated.

Fig. S5 Comparing ISM image reconstructions with adaptive and theoretical shifts.

Fig. S6 ISM reconstruction in axial scan (XZ) mode

Note S1 Real-time reassignment algorithm

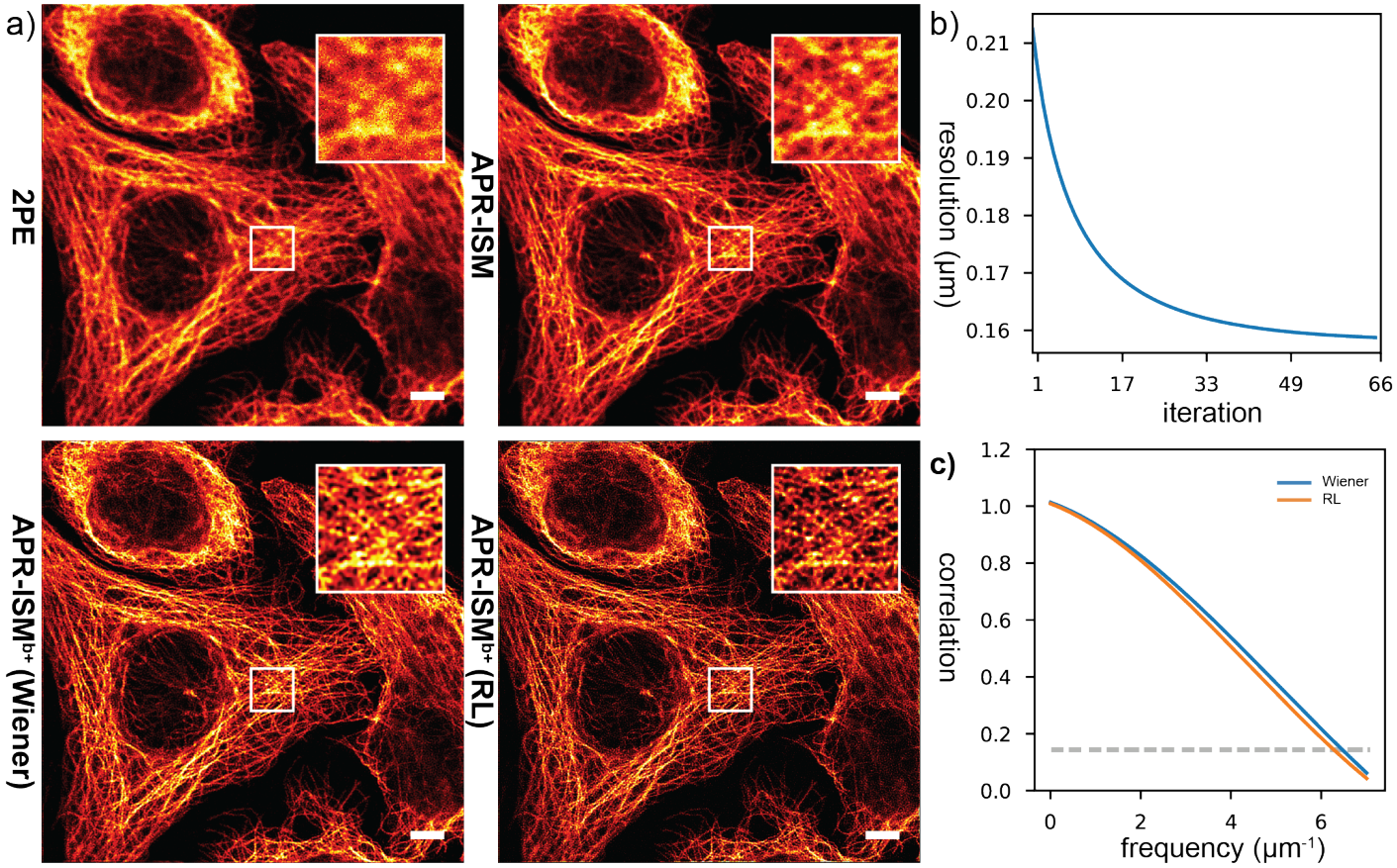

FIG. S 1. **Comparing blind Wiener and Richardson Lucy deconvolution** In a) the performance of the blind Wiener filtering is compared against iterative Richardson-Lucy (RL) deconvolution. The RL algorithm produces sharper looking results with strongly improved contrast, but quantitatively, as shown by FRC measurements in c), the resolution in the two images is the same. It may thus be beneficial to use RL or other iterative algorithm to produce the crispiest looking results, but as shown in b) it takes about 50 iterations for the RL algorithm to reach the same resolution scale the the Wiener filter is able to produce with a single division. Thus, when speed is an issue, Wiener filter provides a much superior solution (of course RL can be significantly accelerated with GPU if necessary). Scale bar 4 μm.

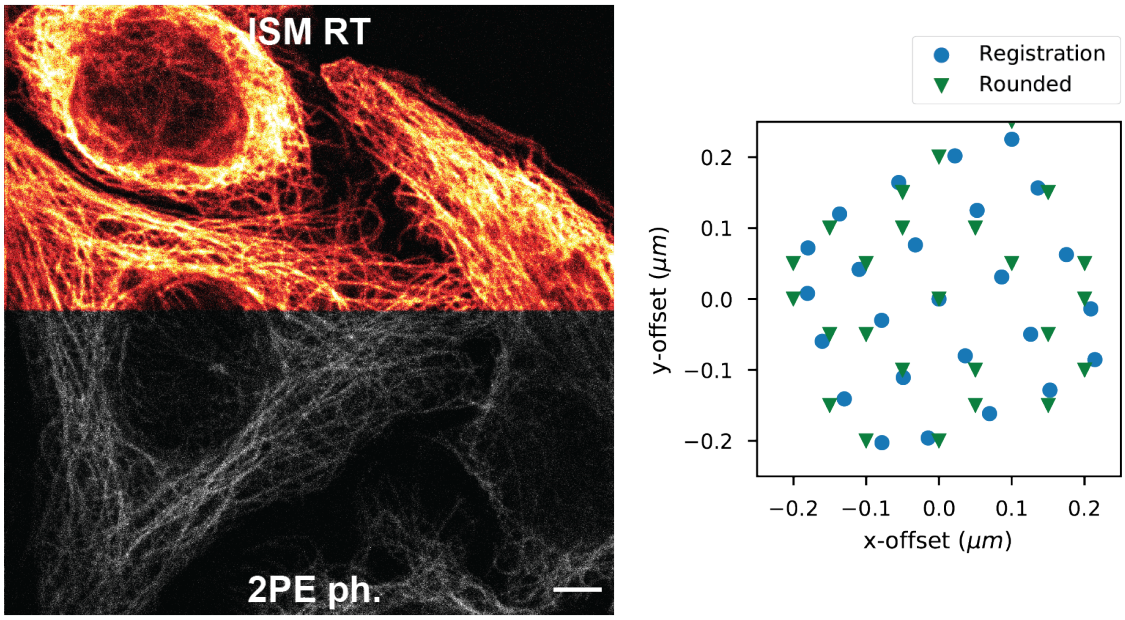

FIG. S 2. **Real-time pixel-reassignment in action**. Real-time pixel reassignment is shown to dramatically boost the SNR in the HeLa cell image, when compared to 2PE image with a pinhole. This makes it possible to achieve the resolution gain (and optical sectioning capability) in practice that the small pinhole can in theory provide. In the scatter plot ISM shifts discretized to multiples of the pixel size (Note S 1) are compared to the actual registration results. The discretized shifts are used by the real-time pixel reassignment algorithm, because no re-sampling is performed, but simple array indexing is used instead. While the rounding does produce small errors, the observed image quality still remains high. Scale bar 4 μm.

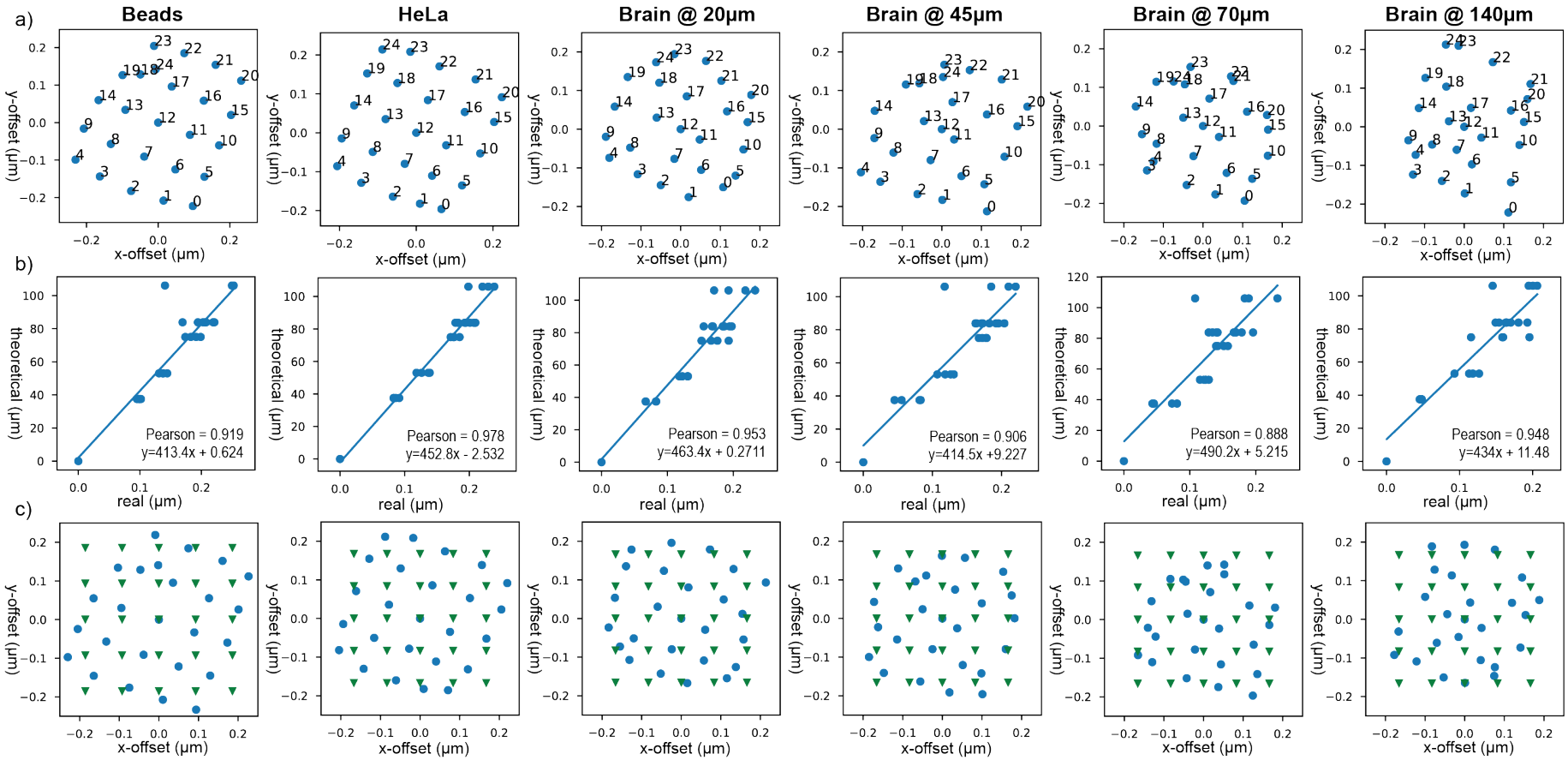

FIG. S 3. **Comparing theoretical and data-based ISM shifts.** In a) scatter plots of the registration results (ISM shifts) for all the images of the main article are shown. In b) the lengths of the data-based shifts (from a)) compared with theoretical, optical geometry based values (Fig. S 4). The *theoretical* shifts are shown as distances on the detector plane, whereas the *real* distances are on the object plane – therefore the slope of the linear model fit roughly reflects the total magnification of the microscope. The *theoretical* and *real* values increase rather linearly with the thin test samples, but the differences increase in the brain sample images. As shown in c), in all cases, the theoretical shifts (green triangles) on a 2D plane never even closely match the real ones (blue circles), as the various optical effects are not accounted for.

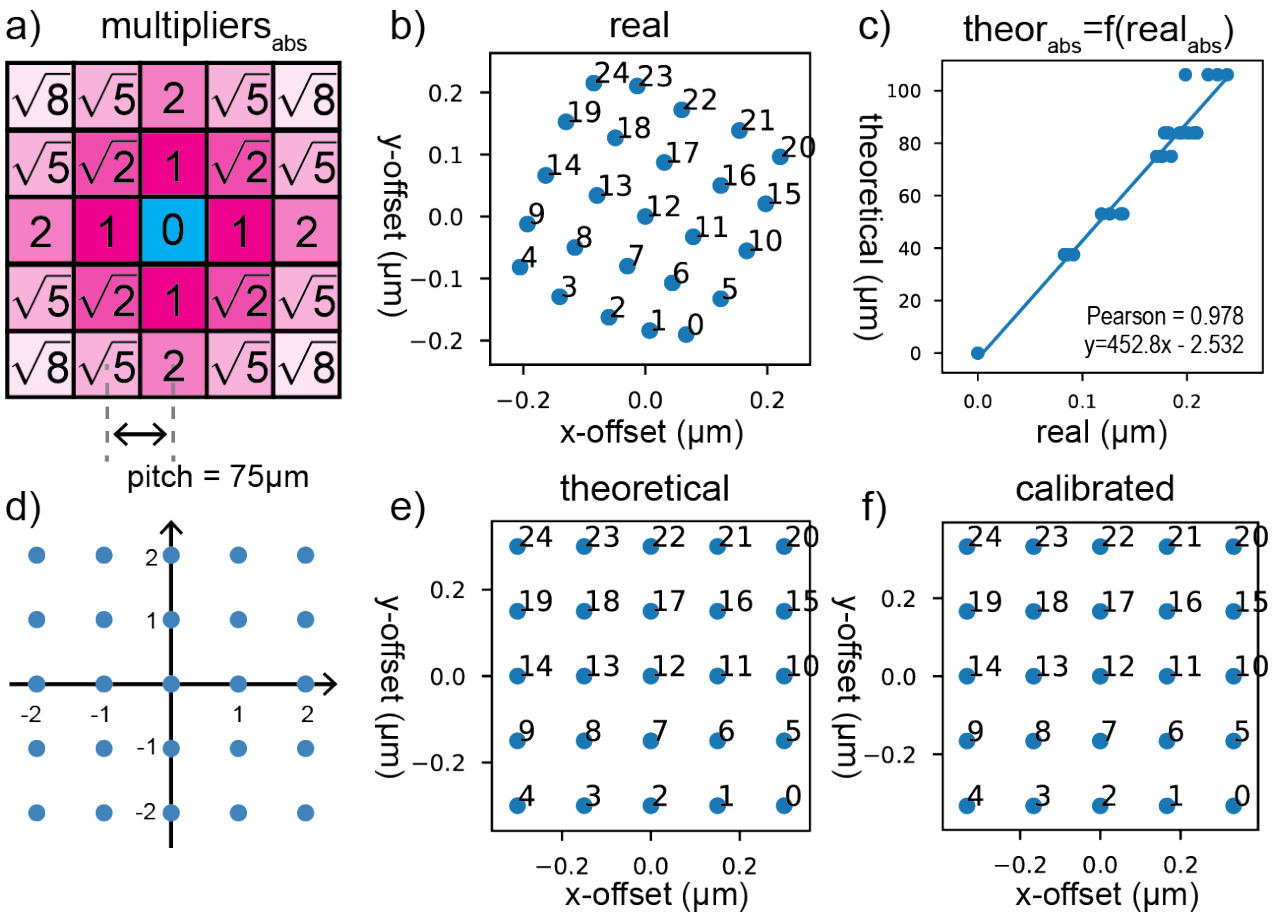

FIG. S 4. **Describing how theoretical ISM shifts are calculated.**. The SPAD array is a 5x5 square detector grid with 75 μm detector pitch. For every pixel (detector element), absolute distance from the center (pixel 12) can be calculated with the multipliers shown in a). The length of the theoretical ISM shifts on the detector plane (theor$_{abs}$), can be obtained by further multiplying the pixel offsets with the reassignment factor (0.5 here). Plotting the theoretical shifts as a function of length of the real ISM shifts on the object plane (real$_{abs} = \sqrt{x^2 + y^2}$, for all (x,y) pairs in b)), allows us to estimate the effective magnification in the microscope from the slope of the linear model fit in c). Theoretical and calibrated ISM shifts were generated by first creating a 5x5 meshgrid d), and then, in order to have the shifts in physical units (μm) on the object plane, multiplying the grid coordinates by $\frac{\text{pitch}\cdot\text{reassignment factor}}{\text{magnification}}$ in e) and $\frac{\text{pitch}\cdot\text{reassignment factor}}{\text{slope}}$ in f), where slope denotes the slope of the linear model fit in c).

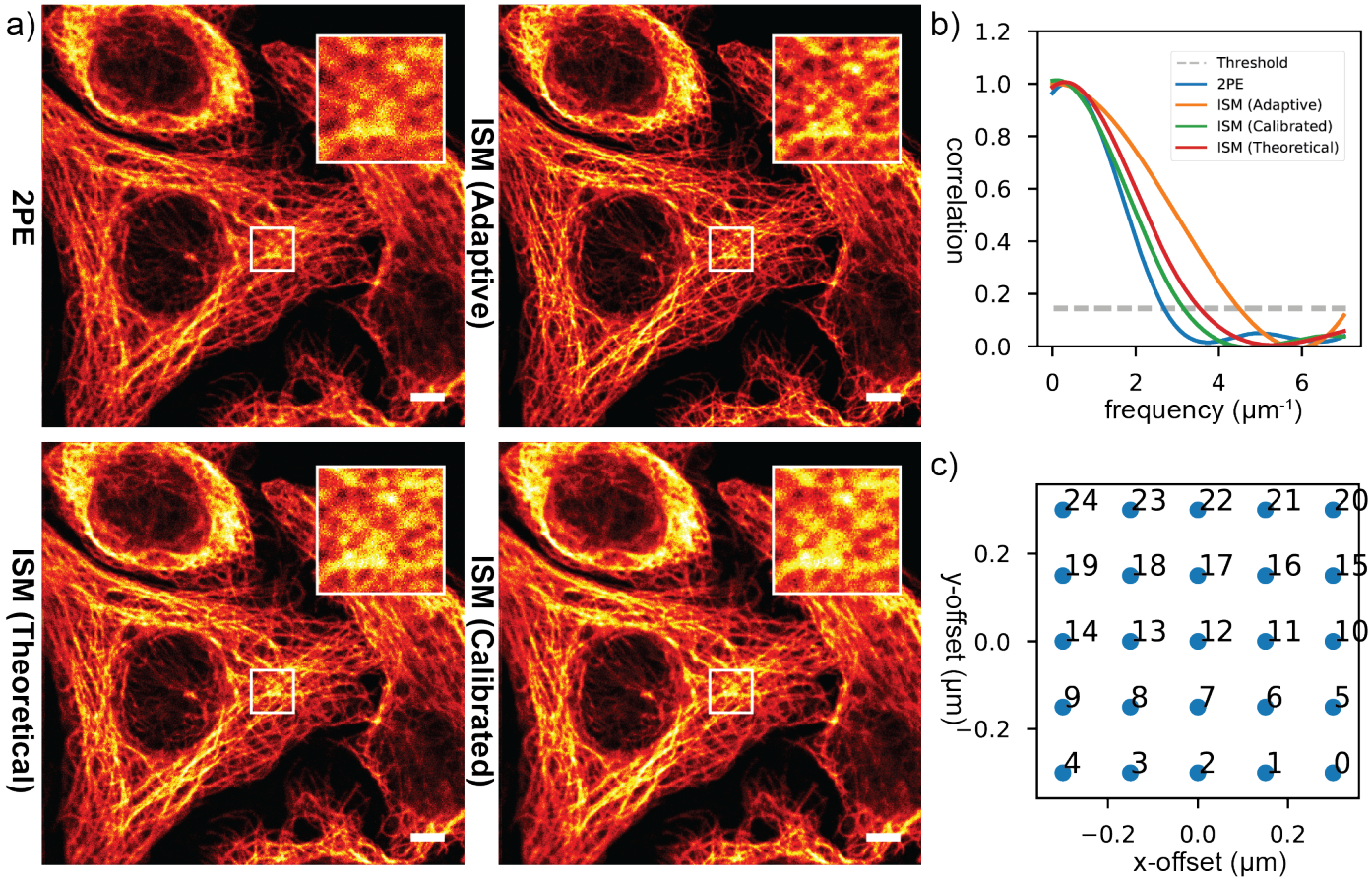

FIG. S 5. **Comparing ISM image reconstructions with adaptive and theoretical shifts.** ISM reconstructions are shown for the HeLa cell image with adaptive, theoretical and calibrated shifts; the theoretical and calibrated shifts were obtained, as illustrated in (Fig. S 4). The adaptive ISM reconstruction produces clearly superior results. Scale bar 4 μm.

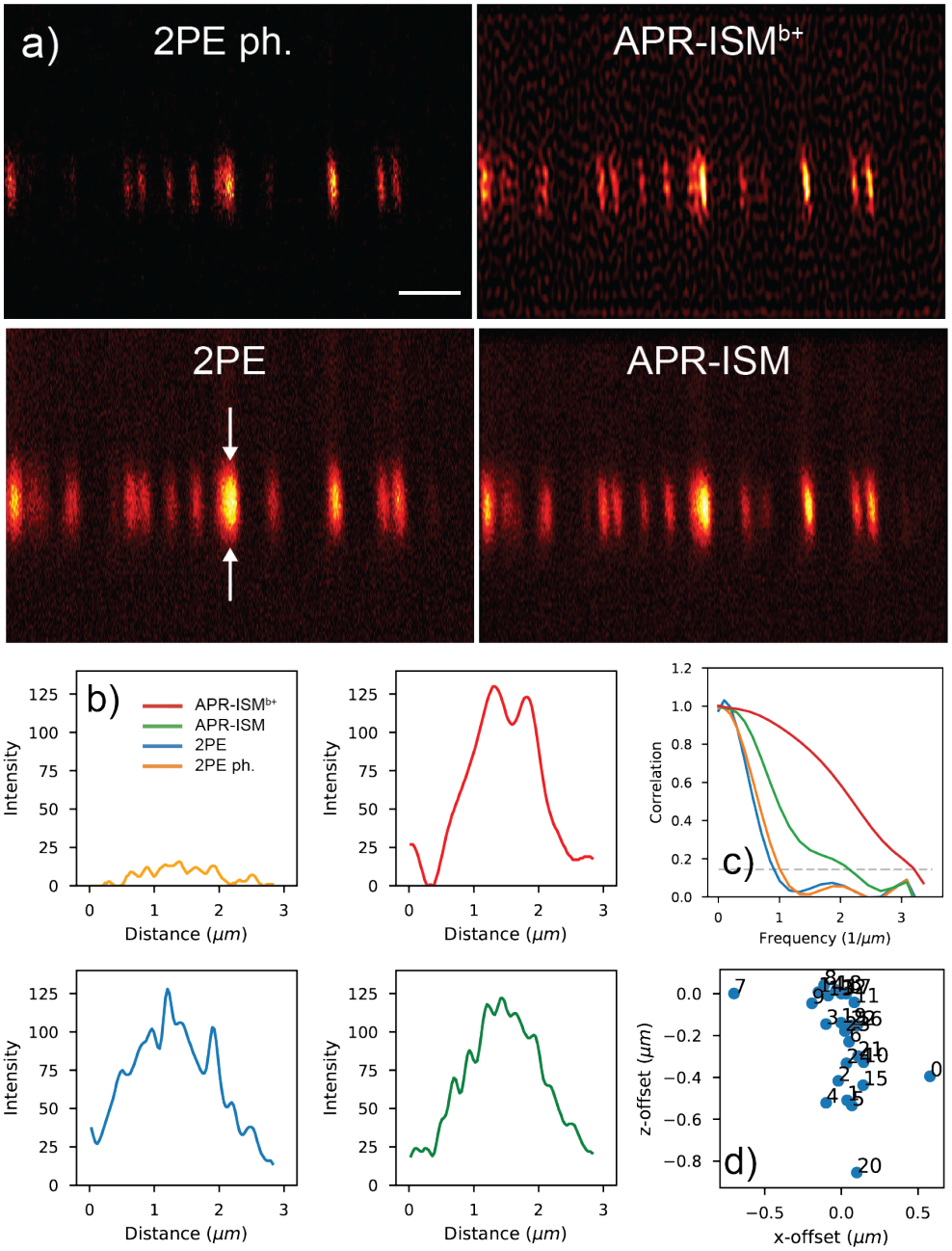

FIG. S 6. **ISM reconstruction in axial scan (XZ) mode**. In a), results of ISM image reconstruction of a single axial XZ slice with the nanoparticle sample are shown. From a) it is evident that APR-ISM clearly improves the resolution of the regular 2PE both in the axial and the lateral dimension. A strong signal gain (> 6 fold) is made with respect to the 2PE ph, which enables the strongly increased effective resolution. Line profile plots in the axial direction over the large cluster highlighted in a), show a clear axial resolution gain. In APR-ISM^{b+} several structures are clearly visible both in axial and lateral directions. In the Wiener filtering, a oval-shaped PSF ($\sigma_x = 0.2\ \mu m, \sigma_z = 0.53\ \mu m$) was used. FRC measurements in c) also confirm the observed resolution gain. The image shifts shown in d) are rather surprising: very strong shifts are present in z as well. Scale bar 2 μm.

Note S 1. Real-time ISM pixel reassignment algorithm

Our real-time pixel reassignment algorithm is shown in (Algorithm S 1). Image of size $(imageWidth, imageHeight)$ is formed one sampling position at a time, typically by laser-scanning. At each sampling position $(column, row)$ the photon counts from each pixel of the array detector are added to the correct position in the $resultImage$, by applying the image shifts $(shiftsY, shiftsX)$. The image shifts can be based on image registration results of the previous frames, or alternatively theoretical values can be used. In order to perform the reassignment in real-time, the $(shiftsY, shiftsX)$ need to be expressed as pixels in stead of physical distances, which means that they have to be rounded to multiples of the pixel size. This can create a small error in the shifts as shown in (Fig. S2), but in most cases this should not be an issue. It is possible to scale the result image to a smaller pixel size than the sampling grid, if necessary, to account for the higher resolution and to decrease the shift error. In (Algorithm S 1) this would simply involve creating a larger result image, and scaling the shifts by the ratio of the sampling grid and the result image pixel sizes.

Algorithm S 1 Simple pseudocode for our real-time pixel reassignment algorithm. Words in italics denote variable names.

```
resultImage ← zeros((imageHeight, imageWidth))
for column in range(imageWidth) do
  for row in range(imageHeight) do
    arrayData ← GetPhotonCounts()
    for detector in range(nDetectors) do
      pixel ← arrayData[detector]
      xIdx ← int(column − shiftsX[detector])
      yIdx ← int(row − shiftsY[detector])
      if xIdx ≥ 0 and xIdx < imageWidth and yIdx ≥ 0 and yIdx < imageHeight then
        resultImage[yIdx, xIdx] += pixel
      end if
    end for
  end for
end for
```